Coherent x-ray magnetic imaging with 5 nm resolution

Riccardo Battistelli, Daniel Metternich, Michael Schneider, Lisa-Marie Kern, Kai Litzius, Josefin Fuchs, Christopher Klose, Kathinka Gerlinger, Kai Bagschik, Christian M. Günther, Dieter Engel, Claus Ropers, Stefan Eisebitt, Bastian Pfau, Felix Büttner, Sergey Zayko

Angaben zur Veröffentlichung / Publication details:

Battistelli, Riccardo, Daniel Metternich, Michael Schneider, Lisa-Marie Kern, Kai Litzius, Josefin Fuchs, Christopher Klose, et al. 2024. "Coherent x-ray magnetic imaging with 5 nm resolution." *Optica* 11 (2): 234–37. https://doi.org/10.1364/optica.505999.

OPTICA

Coherent x-ray magnetic imaging with 5 nm resolution

Riccardo Battistelli,[1,2] Daniel Metternich,[1,2] Michael Schneider,[3] Lisa-Marie Kern,[3] Kai Litzius,[2] Josefin Fuchs,[3] Christopher Klose,[3] Kathinka Gerlinger,[3] Kai Bagschik,[4] Christian M. Günther,[5] Dieter Engel,[3] Claus Ropers,[6,7] Stefan Eisebitt,[3,8] Bastian Pfau,[3] Felix Büttner,[1,2,*] and Sergey Zayko[6,7]

[1]Helmholtz-Zentrum Berlin, 14109 Berlin, Germany
[2]Experimental Physics V, Center for Electronic Correlations and Magnetism, University of Augsburg, 86159 Augsburg, Germany
[3]Max Born Institute for Nonlinear Optics and Short Pulse Spectroscopy, 12489 Berlin, Germany
[4]Deutsches Elektronen-Synchrotron (DESY), 22607 Hamburg, Germany
[5]Technische Universität Berlin, Zentraleinrichtung Elektronenmikroskopie (ZELMI), 10623 Berlin, Germany
[6]Department of Ultrafast Dynamics, Max Planck Institute for Multidisciplinary Sciences, 37077 Göttingen, Germany
[7]4th Physical Institute, University of Göttingen, 37077 Göttingen, Germany
[8]Technische Universität Berlin, Institut für Optik und Atomare Physik, 10623 Berlin, Germany
*felix.buettner@helmholtz-berlin.de

Received 14 September 2023; revised 14 December 2023; accepted 14 December 2023; published 7 February 2024

Soft x-ray microscopy plays an important role in modern spintronics. However, the achievable resolution of most x-ray magnetic imaging experiments limits access to fundamental and technologically relevant length scales in the sub-10 nm regime. Here, we demonstrate x-ray magnetic microscopy with 5 nm resolution by combining holography-assisted coherent diffractive imaging with heterodyne amplification of the weak magnetic signal. The gain in resolution and contrast makes magnetic pinning sites visible and allows to measure the local width of domain walls. The ability to detect and map such properties with photons opens new horizons for element-specific, time-resolved, and *operando* research on magnetic materials and beyond.

https://doi.org/10.1364/OPTICA.505999

Nanometer-scale textures are ubiquitous in nature and can emerge due to competing interactions [1], topological constraints, or pinning at defects. In the realm of magnetism, prominent examples are domain walls, vortices, and skyrmions in two dimensions, and even richer topological configurations in three dimensions [2]. These objects are subject of intense research because of their exciting physics and potential use in low-energy, high-performance information and sensing technologies [3].

Progress in this field relies on high-resolution imaging techniques such as Lorentz microscopy, scanning probe, or magneto-optical methods [4]. In this context, soft x-ray imaging methods stand out as *operando* techniques because they allow to combine nanometer spatial resolution, pico- to femtosecond temporal resolution, element-specific contrast, large penetration depth, and the ability to study patterned devices during the application of a variety of stimuli [5–10]. X-ray imaging has, for example, enabled the direct observation of spin-orbit torque switching of a magnetic random access memory layer [6], the 3D spin configuration around Bloch points [7], and skyrmions in a compensated ferrimagnet [8]. However, despite advances in this field, achieving a resolution under 20 nm remains challenging, with only exceptional experiments reaching the 7–10 nm mark [5,9,11,12]. Consequently, photon-based microscopy has provided limited information about fundamental and technologically relevant properties of many magnetic materials, such as the width of domain walls and the origin of domain wall pinning.

Here, we advance photon-based magnetic imaging to a resolution of 5 nm already on a third-generation synchrotron-radiation source. Specifically, we employ holography-assisted phase retrieval (HAPRE) [13] using an approach based on two ingredients: first, waveguiding reference holes with strongly modulated exit waves [14,15] to amplify the weak magnetic scattering [16,17] and second, a combination of Fourier transform holography (FTH) [18,19] and phase-retrieval algorithms [20,21]. The method allows to resolve small and low-contrast spin textures including magnetic domain walls and magnetic pinning points in a magnetic multilayer. The results provide a qualitatively new level of understanding of interactions in the broad class of magnetic multilayers, in which heavy metal layers often defy access by surface-sensitive and even electron-based probes.

The sample is a Pt(3)|[Pt(2)|Co(0.8)|Cu(0.5)]$_{15}$|Pt(2) (thicknesses in nm) multilayer grown via direct current magnetron sputtering on a SiN membrane. The material belongs to the class of chiral magnetic multilayers, which are of large interest in the field of spintronics [2,3] since in such materials the combination of perpendicular magnetic anisotropy and Dzyaloshinskii-Moriya interaction (DMI) leads to the emergence of nanometer-scale

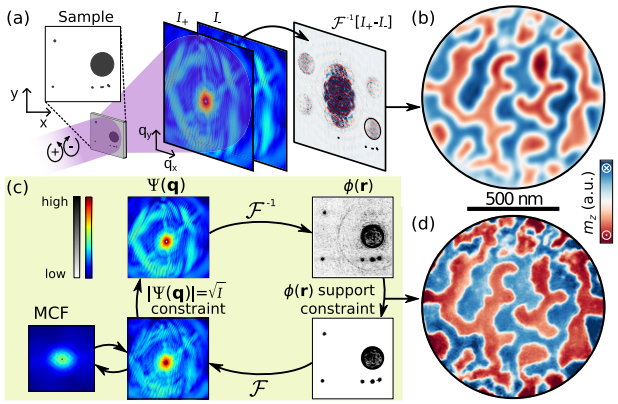

Fig. 1. HAPRE workflow. (a) A coherent x-ray beam of alternating helicity illuminates the sample, resulting in the diffraction patterns $I_\pm$. (b) FTH-reconstructed magnetic image (sample exit wave). (c) Sketch of the phase-retrieval process. (d) Phase-retrieved magnetic image obtained from the reconstruction of both helicities. MCF, mutual coherence function.

magnetic textures. Imaging was performed in a FTH geometry [18] [Fig. 1(a)] at the Co L3 edge (wavelength 1.59 nm) using x-ray magnetic circular dichroism contrast. After illumination with a coherent soft-x-ray beam with positive (+) and negative (−) helicity, the sample exit waves $\phi_\pm(\mathbf{r})$ were computationally reconstructed from the recorded far-field scattering intensity $I_\pm(\mathbf{q}) = |\Psi_\pm(\mathbf{q})|^2$, where $\Psi_\pm(\mathbf{q}) \propto \mathcal{F}[\phi_\pm(\mathbf{r})]$ is the wavefront at the detector ($\mathbf{r}$ is the spatial position and $\mathbf{q}$ the photon momentum transfer vector). To realize FTH, we used a monolithically integrated opaque Cr/Au mask with a 1 μm diameter object hole and reference holes with diameters of 40–60 nm arranged in a pattern optimized for HAPRE [16].

To account for the dynamic range of the diffraction patterns, we recorded and merged data with increasing beam-stop sizes. The data was offset corrected, normalized, and projected onto the Ewald sphere. The FTH mask design allows us to obtain an image ("reconstruction") from a single Fourier transform of the diffraction pattern [Fig. 1(b)] as a convolution between the object and reference hole exit waves. As a consequence, the resolution and contrast of this reconstruction are limited by the reference hole size and shape [18]. However, this relatively low-resolution image is sufficient to accurately determine the support mask needed for phase-retrieval algorithms [Fig. 1(c)], which remove the FTH limitation. We first reconstructed the positive helicity exit wave ϕ_+ with a combination of the relaxed averaged alternating reflections (RAAR) algorithm [20] and error-reduction (ER) algorithm [21]. Then, the negative helicity exit wave ϕ_- was reconstructed employing the ER algorithm using the phase of ϕ_+ as a starting guess. Finally, our routine accounts for partial coherence (e.g., due to low intrinsic spatial coherence of the source, vibrations in the beam path, and contributions of higher harmonics, as known at the beamline [22]) by incorporating a Richardson-Lucy deconvolution algorithm estimating the mutual coherence function of the beam [23]. See Supplement 1 for details.

The local out-of-plane magnetization was extracted as $m_z \propto \log(|\phi_+/\phi_-|)$ (see Supplement 1) and focused numerically by wavefront propagation [15] [Fig. 1(d)]. Note that absolute values for m_z can in principle be obtained, but were inaccessible in our experiment due to higher harmonic contributions at low $\mathbf{q}$ and fluctuations of the illumination [22]. It is expected that the next generation of x-ray sources will address these challenges.

In a mask-based magnetic scattering experiment, the wavefront at the detector, $\Psi_\pm = \Psi_c \pm \Psi_m$, is composed of two terms: the charge scattering of the mask $\{\Psi_c \propto \mathcal{F}[\phi_c(\mathbf{r})]$, where $\phi_c(\mathbf{r})$ is the non-magnetic transmission function of the mask including reference holes$\}$ and the magnetic scattering of the spin texture $\{\Psi_m = \mathcal{F}[\phi_m(\mathbf{r})] \approx \mathcal{F}[\phi_c(\mathbf{r}) m_z(\mathbf{r})]$, where $\phi_m(\mathbf{r})$ is the magnetic component of the exit wave$\}$. The sign (±) changes with the helicity [13,17]. The resulting helicity-dependent intensities, $I_\pm = |\Psi_\pm|^2 = |\Psi_c|^2 + |\Psi_m|^2 \pm 2\mathrm{Re}(\Psi_c \Psi_m)$, contain three terms: a pure charge scattering term, a purely magnetic term, and a heterodyne product between the charge and magnetic components. Notably, this last term is responsible for the dichroic contrast between the diffraction patterns and is linear in Ψ_m, making it best suited to reconstruct the magnetic image. Importantly, $|\Psi_m|$ alone decays as q^{-2} (see Supplement 1) and is therefore particularly weak at high $\mathbf{q}$, where the information from the smallest magnetic features is encoded. Thus, high-resolution magnetic imaging relies on strong charge scattering Ψ_c up to the highest $\mathbf{q}$ to amplify weak magnetic scattering above the instrumental noise level and above the minimum of one photon per speckle.

One way of generating high-$\mathbf{q}$ scattering is by controlled fabrication of sharp features. However, this would tie the achievable resolution to the precision of nanofabrication methods and make high-resolution imaging extremely challenging. Fortunately, reference holes naturally exhibit scattering to high $\mathbf{q}$ (see Supplement 1), owing to the strong field modulations at the exit surface, provided that the narrow section is large and short enough to support high-order guided modes [14,24]. A tapered geometry [15], combined with the multiple scattering within the holes on roughness, inhomogeneities, and material boundaries, can further amplify this effect and provide sub-10 nm period modulations of the exit surface wave. Notably, the combined diffraction pattern from different reference holes covers the entire recorded q range.

The effect of the resulting amplification is visible in Figs. 2(a) and 2(b), which display a comparison of the heterodyne term with and without reference hole contributions (obtained computationally from the reconstructions as described in Supplement 1). Without reference hole scattering, the signal decays strongly with $\mathbf{q}$ and little to no signal is found at the detector edges. With the contribution of reference holes, the heterodyne magnetic signal is significantly amplified [by a factor of 7.4 at $q = \frac{2\pi}{5.3\mathrm{nm}}$; see Fig. 2(b)] and recorded up to the edges of the detector, corresponding to a 5.3 nm resolution of the reconstructions. The signal remains strong even at the detector corners, demonstrating that a resolution of ∼4 nm is in reach with a larger detector. The resolution values are verified with Fourier ring correlation as well as phase-retrieval transfer function measurements [Fig. 2(c)], which additionally demonstrate the robustness of the reconstructed details against statistical noise and variations of the initial guess of the phase, respectively. An analysis of the resolution as a function of the total exposure time reveals that 5 min was sufficient to reach the 5.3 nm mark [Fig. 2(d)], although longer exposures yield higher signal-to-noise ratios.

To identify which magnetic features are newly resolved by the gain in resolution, we show in Figs. 2(e) and 2(f) an image and a line scan of a magnetic domain wall. A fit to the Kittel domain wall profile, $m_z = \tanh(x/\delta)$, yields a full domain wall width of

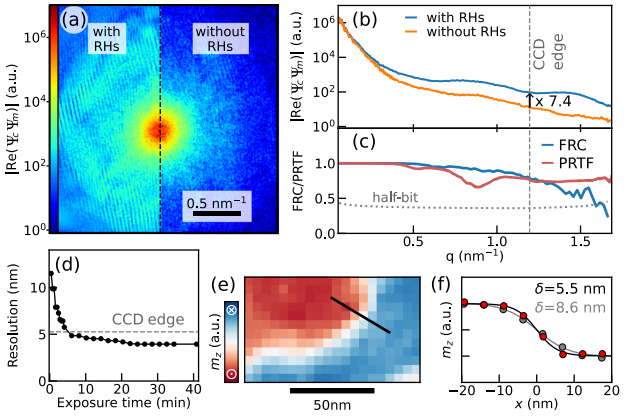

Fig. 2. Demonstration of magnetic imaging with 5 nm resolution. (a) Heterodyne term $2\mathrm{Re}(\Psi_c \Psi_m)$ of the diffraction patterns in Fig. 1 with and without reference hole (RH) contributions. Absolute values are used for improved legibility. (b) Radial averages of the terms in (a). (c) Fourier ring correlation (FRC) and phase-retrieval transfer function (PRTF) of the reconstruction in Fig. 1(d). (d) Resolution versus total exposure time, computed with FRC. (e) Section of Fig. 1(d). (f) Dots: $m_z(x)$ measured along the black line in (e), by interpolation. Line: fit to $m_z(x) = \tanh(x/\delta)$. Faint contrast: same after omitting photons with $q > \frac{2\pi}{15\mathrm{nm}}$. The gray dashed line labeled "CCD edge" marks the $q = \frac{2\pi}{5.3\mathrm{nm}}$ at the edges of the detector. 5.3 nm is the reconstruction pixel size. a.u., arbitrary units.

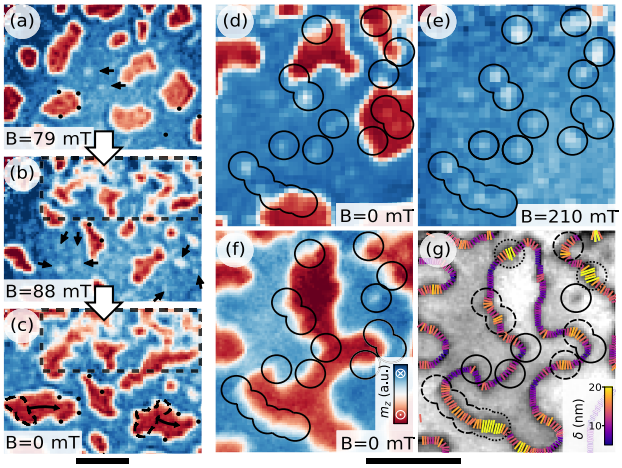

Fig. 3. Imaging of magnetic pinning. (a)–(f) Domain patterns. (g) Domain wall widths of the state in (f). The colored lines in (g) represent the detected domain walls. Each line is centered on and perpendicular to the relative domain wall, and has a length equal to δ. Annotations mark the locations of magnetic pinning points. Details, see text. Scalebar under (c) refers to (a)–(c); scalebar under (f), (g) refers to (d)–(g). Scalebars are 200 nm.

$\pi\delta = 17$ nm ($\delta = 5.5$ nm). This is in close agreement with micromagnetic simulations of our material (predicting $\delta = 5.1$ nm). Importantly, although the full width is three times larger than our resolution, the domain wall broadens when omitting the highest **q** photons [5]. A detailed analysis (Supplement 1) shows that a resolution of $\sim\delta$ is needed to accurately resolve a Kittel domain wall profile. The measured value of δ thus supports our resolution estimate in real space and shows that the obtained resolution is key for quantitative magnetic materials science.

Moreover, the enhanced contrast and resolution reveal features previously invisible in photon-based magnetic imaging experiments. As we demonstrate next, this allows HAPRE to address a long-standing challenge in materials science: to reveal the location and mechanism of magnetic pinning – the ubiquitous phenomenon that magnetic textures get pinned at certain locations in the material [10,25].

As an example, we study magnetic pinning in our multilayer after fs laser exposure. This choice is motivated by the wide interest in laser-induced ultrafast dynamics in chiral materials and by the importance of understanding laser-induced damage and pinning in this context [26]. In a first experiment, we imaged the domain state with an image pixel size of 10 nm. Figures 3(a)–3(c) display a section of the experimental field of view after various levels of exposure to a 1030 nm fiber laser with 250 fs pulses. Moderate laser exposure (10 pulses, fluence 52 mJcm^{-2} at $B_z = 79$ mT magnetic field) led to the anticipated nucleation of isolated domains [Fig. 3(a)]. However, more intense laser exposure (100 pulses, fluence 68 mJcm^{-2}, $B_z = 88$ mT) additionally resulted in large damaged areas characterized by smaller domains and reduced magnetic contrast [Figs. 3(b) and 3(c), sections delimited by the black dashed line]. The subsequent removal of the magnetic field led to the expansion of magnetic domains [Fig. 3(c)]. Throughout this sequence of magnetic states, the presence of pinning sites can be inferred by identifying locations where domain walls repeatedly come to rest or form cusps, as indicated by black dots. In the same locations, we observe objects with magnetic contrast in between the values of the up and down magnetized domains (see black arrows), suggesting direct visibility of pinning sites even in the absence of a domain wall. However, their faint contrast makes precise verification challenging.

The signal-to-noise ratio can be increased with longer exposure times, as shown in Figs. 3(d) and 3(e) for a different field of view of the same sample. This allows to robustly detect the low-contrast features and confirm their magnetic nature from their alternating contrast in single helicity reconstructions (see Supplement 1). Yet another level of insight is reached by increasing the numerical aperture of the setup by moving the detector closer to the sample, which increases the resolution to 5 nm and thereby enables measurements of the local δ [Figs. 3(f) and 3(g)]. This allows us to explore correlations between domain wall pinning, low-contrast features, and variations in domain wall width.

To this end, we imaged the sample at remanence [Fig. 3(d)], following a partial demagnetization cycle that promoted domain rearrangement [Fig. 3(f)], and under an external field of 210 mT [Fig. 3(e)]. The low-contrast features consistently appeared in the same positions on multiple images [for example, see circles in Figs. 3(d) and 3(e), taken at different beamtimes] and were not annihilated by the external field, indicating a strong connection to specific locations. Domain walls are generally attracted to these locations of low-contrast features [e.g., Fig. 3(f)]. These observations are consistent with a recent report of small, low-magnetization spots acting as pinning points in $CrBr_3$ bilayers, as observed using NV center scanning magnetometry, although without fully resolving the magnetization pattern [27]. In this context, it is most remarkable that the measurement of δ reveals a highly non-trivial relationship: in some cases the δ at a defect is comparable to defect-free regions of the sample (solid circles), while in others the domain walls are larger (dashed circles), with values exceeding 20 nm (dotted circles) [Fig. 3(g)].

To understand these results, we recall that the domain wall width $\pi\delta$ and the domain wall energy σ in chiral magnetic

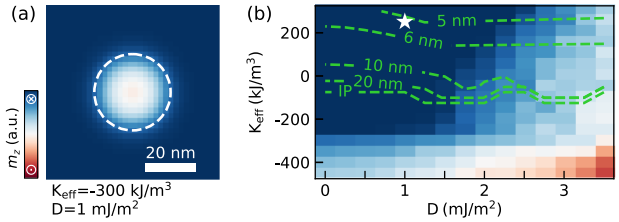

Fig. 4. Micromagnetic simulations of pinning points. (a) Example of a magnetic state in a low-anisotropy defect (delimited by the dashed line). (b) Phase space of m_z found at the center of the defect, as a function of K_{eff} and D. White star: defect-free region of material. Green lines: dependence of δ on K_{eff} and D in a uniform magnetic material.

materials are in first approximation given by $\delta \approx \sqrt{A/K_{\text{eff}}}$ and $\sigma = 4\sqrt{AK_{\text{eff}}} - \pi|D|$ [28]. Here, D is the DMI strength, K_{eff} is the effective out-of-plane anisotropy constant, and A is the exchange stiffness. In multilayer materials, both D and K_{eff} can easily be affected by growth conditions and post-growth treatment [26,29,30]. Local variations of these parameters explain the presence of attractive pinning points in the material [31], as an increase in D or a reduction in K_{eff} would lower the domain wall energy density σ. Furthermore, δ would increase with lower K_{eff} while being independent of D, as confirmed with micromagnetic simulations [Fig. 4(b)]. Therefore, localized independent variations of K_{eff} and D are both plausible and explain the variety of domain wall widths observed experimentally at pinning sites in Fig. 3(g): while high-DMI defects attract domain walls without affecting their width, low-anisotropy defects also increase δ.

To understand how these defects would also be directly visible as points with lower magnetic contrast, we performed micromagnetic simulations using the Mumax3 solver [32]. The bulk of the material was modeled with magnetic parameters derived from experimental data and literature, while the K_{eff} and D were altered inside a circular defect of 30 nm in diameter. The simulations were started from a random magnetization and relaxed under an external field of 210 mT. After relaxation, the major part of the sample is saturated, while for certain K_{eff} and D the defect stabilizes spin textures locally lowering m_z at its center [Fig. 4(a)]. Systematic exploration of the anisotropy-DMI phase space [Fig. 4(b)] reveals that a local reduction of m_z is achieved if within the defect either K_{eff} is lowered or D is increased. The same trends also lower the domain wall energy, explaining why low-contrast features act as domain wall pinning sites.

We have demonstrated x-ray magnetic imaging with a record-high 5 nm resolution using holography-assisted phase retrieval. A verified resolution of ~4 nm is immediately in reach with larger detectors. Key to this ability is the heterodyne mixing of magnetic scattering with strong charge scattering at high **q**, achievable with a bright reference beam exhibiting nanometer-scale field modulations. Our high-resolution images resolve the structure of magnetic domain walls, make magnetic pinning points directly visible, and allow to investigate the underlying pinning mechanisms. These capabilities lift photon-based magnetic microscopy to a qualitatively new level. Most importantly, the technique leverages the emergence of high-coherence x-ray sources around the world, where sub-wavelength spatial resolution (as demonstrated in the extreme-UV regime [16]) comes into reach, thereby finally extending x-ray magnetic imaging to the fundamental length scales as defined by the exchange interaction. Finally, our technique is compatible with time-resolved coherent imaging [10,16] and is directly applicable to a broad range of low-contrast material systems and phenomena, ranging from biological samples to the direct imaging of the structural and chemical transitions, granted by compatibility with spectroscopic contrast at any photon energy.

Funding. Helmholtz Young Investigator Group Program (VH-NG-1520); Leibniz-Gemeinschaft ((OptiSPIN), K162/2018).

Acknowledgment. We acknowledge DESY. This research was carried out at PETRA III at the P04 beamline.

Disclosures. The authors declare no conflicts of interest.

Data availability. Data underlying the results presented in this paper are available in Dataset 1, Ref. [33].

Supplemental document. See Supplement 1 for supporting content.

REFERENCES

1. M. Seul and D. Andelman, Science **267**, 476 (1995).
2. B. Göbel, I. Mertig, and O. A. Tretiakov, Phys. Rep. **895**, 1 (2021).
3. H. Vakili, J.-W. Xu, W. Zhou, *et al.*, J. Appl. Phys. **130**, 070908 (2021).
4. R. M. Reeve, H.-J. Elmers, F. Büttner, *et al.*, *Magnetic Imaging and Microscopy* (Springer, 2021), pp. 1–52.
5. X. Shi, P. Fischer, V. Neu, *et al.*, Appl. Phys. Lett. **108**, 094103 (2016).
6. M. Baumgartner, K. Garello, J. Mendil, *et al.*, Nat. Nanotechnol. **12**, 980 (2017).
7. C. Donnelly, M. Guizar-Sicairos, V. Scagnoli, *et al.*, Nature **547**, 328 (2017).
8. L. Caretta, M. Mann, F. Büttner, *et al.*, Nat. Nanotechnol. **13**, 1154 (2018).
9. W. Li, I. Bykova, S. Zhang, *et al.*, Adv. Mater. **31**, 1807683 (2019).
10. C. Klose, F. Büttner, W. Hu, *et al.*, Nature **614**, 256 (2023).
11. A. P. Hitchcock, J. Electron Spectrosc. Relat. Phenom. **200**, 49 (2015).
12. A. Rana, C.-T. Liao, E. Iacocca, *et al.*, Nat. Nanotechnol. **18**, 227 (2023).
13. O. Kfir, S. Zayko, C. Nolte, *et al.*, Sci. Adv. **3**, eaao4641 (2017).
14. S. Zayko, E. Mönnich, M. Sivis, *et al.*, Opt. Express **23**, 19911 (2015).
15. E. Malm, B. Pfau, M. Schneider, *et al.*, Opt. Express **30**, 38424 (2022).
16. S. Zayko, O. Kfir, M. Heigl, *et al.*, Nat. Commun. **12**, 6337 (2021).
17. C. Klose, F. Büttner, W. Hu, *et al.*, Phys. Rev. B **105**, 214425 (2022).
18. S. Eisebitt, J. Lüning, W. F. Schlotter, *et al.*, Nature **432**, 885 (2004).
19. S. Flewett, C. M. Günther, C. V. K. Schmising, *et al.*, Opt. Express **20**, 29210 (2012).
20. D. R. Luke, Inverse Probl. **21**, 37 (2005).
21. J. R. Fienup, Appl. Opt. **21**, 2758 (1982).
22. K. Bagschik, J. Wagner, R. Buß, *et al.*, Opt. Express **28**, 7282 (2020).
23. J. Clark, X. Huang, R. Harder, *et al.*, Nat. Commun. **3**, 993 (2012).
24. M. Osterhoff and T. Salditt, New J. Phys. **13**, 103026 (2011).
25. R. Gruber, J. Zázvorka, M. A. Brems, *et al.*, Nat. Commun. **13**, 3144 (2022).
26. M. Stärk, F. Schlickeiser, D. Nissen, *et al.*, Nanotechnol **26**, 205302 (2015).
27. Q.-C. Sun, T. Song, E. Anderson, *et al.*, Nat. Commun. **12**, 1989 (2021).
28. A. Thiaville, S. Rohart, E. Jué, *et al.*, Europhys. Lett. **100**, 57002 (2012).
29. G. A. Bertero and R. Sinclair, MRS Proc. **343**, 369 (1994).
30. M. C. H. de Jong, M. J. Meijer, J. Lucassen, *et al.*, Phys. Rev. B **105**, 064429 (2022).
31. F. Hellman, A. Hoffmann, Y. Tserkovnyak, *et al.*, Rev. Mod. Phys. **89**, 025006 (2017).
32. A. Vansteenkiste, J. Leliaert, M. Dvornik, *et al.*, AIP Adv. **4**, 107133 (2014).
33. R. Battistelli, D. Metternich, M. Schneider, *et al.*, "Dataset for 'Coherent x-ray magnetic imaging with 5 nm resolution'," Zenodo, 2023, https://doi.org/10.5281/zenodo.10149177.